Advanced Materials

ADVANCED MATERIALS
www.advmat.de

RESEARCH ARTICLE OPEN ACCESS

High-Gain Ag_2Te/MoS_2 Hybrid Photodetectors for Short-Wave Infrared Imaging

Seock-Jin Jeong[1,2] | Hyun Woo Ko[3,4] | Suyeon Jo[3,5] | Joicy Selvaraj[1] | Jung-Min Kim[1] | Namji Lee[1] | Jae-Hyeon Ahn[1] | Hyeonchae Lee[1] | Seungmin Jeong[6,7] | Heedae Kim[6,7] | Paul Hongsuck Seo[4] | Jae Won Shim[5] | Yonghun Kim[2] | Hyun-Soo Ra[8] | Min-Chul Park[3,4,5] | Jong-Soo Lee[1,9]

[1]Department of Energy Science & Engineering, Daegu Gyeongbuk Institute of Science & Technology (DGIST), Daegu, Republic of Korea | [2]Energy & Environment Materials Research Division, Korea Institute of Materials Science (KIMS), Changwon, Republic of Korea | [3]Center for Quantum Technology, Post-Silicon Semiconductor Institute, Korea Institute of Science and Technology (KIST), Seoul, Republic of Korea | [4]Department of Computer Science and Engineering, Korea University, Seoul, Republic of Korea | [5]School of Electrical Engineering, Korea University, Seoul, Republic of Korea | [6]Department of Semiconductor Science & Technology, Jeonbuk National University, Jeonju, Republic of Korea | [7]Research Institute for Materials and Energy Sciences, Jeonbuk National University, Jeonju, Republic of Korea | [8]School of Electronics Engineering, Kyungpook National University, Daegu, Republic of Korea | [9]Energy Science and Engineering Research Center, Daegu Gyeongbuk Institute of Science and Technology (DGIST), Daegu, Republic of Korea

Correspondence: Hyun-Soo Ra (hsra@knu.ac.kr) | Min-Chul Park (minchul@kist.re.kr) | Jong-Soo Lee (jslee@dgist.ac.kr)

Received: 23 October 2025 | **Revised:** 3 March 2026 | **Accepted:** 14 March 2026

Keywords: array-driven imaging | hybrid photodetector | hybrid structure | infrared | quantum dot | transition metal dichalcogenide

ABSTRACT

Physical artificial intelligence has emerged as a pivotal component in next-generation humanoid technologies, including advanced optical sensors, as it enables autonomous acquisition of sensory information. This study reports a high-performance 0D/2D hybrid photodetector using a high-gain Ag_2Te/MoS_2 hybrid structure for visible to short-wave infrared (SWIR) photodetection, achieved by the absorption of Ag_2Te quantum dots in the infrared region (~1450 nm). The Ag_2Te/MoS_2 photodetector exhibits a high photoresponsivity of around 7.5×10^5 AW^{-1} and a specific detectivity of over 9.9×10^8 Jones at 1 μW/cm^2 illumination power with a 0.2 V drain bias voltage. Furthermore, depending on the gain of the photodetector, a fast response speed can also be achieved, with rise and decay times as short as 13 and 23 ms. The 0D/2D hybrid devices were successfully implemented in a 32×32 array format for infrared imaging, with the results demonstrating spatially resolved pattern reconstruction and real-time photoresponse acquisition. By hybridizing quantum dots and 2D materials, the developed photodetector has broad potential applications, including use in highly integrated SWIR image sensors.

1 | Introduction

Infrared colloidal quantum dots (IR CQDs) are semiconductor nanocrystals that possess the ability to absorb and emit light in the IR region. Owing to their size-dependent optical and electronic properties, IR CQDs offer tunable bandgaps and thus allow precise control over their IR absorption and emission characteristics by adjusting particle size, composition, and surface modifications [1–8]. IR CQDs such as those based on Ag_2Te, PbS, InSb, InAs, and HgTe have gained significant attention for a wide range of applications, including IR photodetectors, thermal imaging, telecommunications, and biomedical imaging [1, 6, 7, 9–14]. These QDs are especially valuable for enhancing the sensitivity and efficiency of devices operating in the IR range by providing the advantages of flexibility in device design, cost-effectiveness, and

Seock-Jin Jeong, Hyun Woo Ko, and Suyeon Jo contributed equally to this work.

potential integration into existing Si and InGaAs-based electronic systems [5, 8, 14, 15].

In particular, colloidal silver telluride quantum dots (Ag_2Te QDs) are a class of semiconductor nanocrystals that present unique optoelectronic properties and potential applications across wide technological fields [4, 10, 16, 17]. The narrow bandgap of Ag_2Te QDs, which are a Cd-, Pb-, and Hg-free eco-friendly material that complies with EU-RoHS regulations, provides strong IR light harvesting characterized by a high absorption coefficient, enhancing their potential for IR sensing and energy harvesting technologies [17, 18]. Ongoing research is focused on optimizing their synthesis, improving stability, and enhancing performance for practical implementation in next-generation optoelectronics [3, 10, 19].

One emerging class of optoelectronic devices is 0D/2D hybrid IR photodetectors, which combine 0D nanomaterials, such as quantum dots or nanoparticles, with 2D materials like graphene, transition metal dichalcogenides, or black phosphorus [20–24]. This hybrid structure exploits the unique advantages of both material types: 0D nanomaterials provide strong light absorption and size-tunable electronic properties, while 2D materials offer high carrier mobility, flexibility, and excellent surface-to-volume ratios [25–28]. By integrating these properties, 0D/2D hybrid photodetectors achieve enhanced IR detection capabilities, including high sensitivity, fast response times, and tunable detection ranges [19, 23, 24, 29–33]. Related devices have accordingly shown great promise in various applications where efficient IR sensing is critical, such as thermal imaging, night vision, environmental monitoring, and medical diagnostics [25, 34, 35]. However, major challenges remain for scaling up prototype image sensors, including the achievement of homogeneous, wafer-scale integration of 2D materials, the mass production of environmentally benign QDs, and the interfacial ligand engineering required for their coupling.

Here, we report the first proof-of-concept demonstration of a short-wave infrared (SWIR) image sensor employing a 0D/2D hybrid structure. In this architecture, SWIR-sensitive Ag_2Te QDs are integrated with metal–organic chemical vapor deposition (MOCVD)-grown MoS_2 to synergistically combine broadband photon absorption and efficient carrier transport. The optical properties, band alignment, and photogenerated carriers in the 0D/2D hybrid structure were first verified through UV–Vis–IR spectroscopy and ultraviolet photoelectron spectroscopy (UPS). The characterization exhibits how the Ag_2Te QDs leverage the photodoping effect that occurs by transporting photogenerated carriers into MoS_2, providing in-depth insights into exciton diffusion, 0D/2D hybrid gain, and optical response behavior based on the channel length and exciton lifetime. The developed Ag_2Te/MoS_2 photodetector is shown to achieve a high responsivity up to 7.5×10^5 AW^{-1} and high specific detectivity exceeding 9.9×10^8 Jones. Furthermore, we developed a scalable fabrication process for the high-performance hybrid sensors, and successfully demonstrated here the next phase of 0D/2D photodetector research in the form of a 32 × 32 pixel image sensor. Integrating the image sensor with signal-processing and readout integrated circuits (ROICs) will offer the capability to perform high-performance IR imaging.

2 | Results and Discussion

In 0D materials, quantum confinement dominates along all three spatial axes (x, y, and z), allowing facile bandgap tuning and yielding high quantum efficiency in exciton generation under optical excitation. In contrast, 2D materials exhibit strong covalent bonding within the *xy* plane, while the layers are coupled only through van der Waals interactions along the *z*-axis. This results in quantum confinement being limited to the out-of-plane direction, thus enabling high in-plane charge carrier mobility. Combining the advantages of both Dimensionalities, we adopt a hybrid 0D/2D structure in this work to overcome the limited charge transport of QDs while extending the absorption range of the photodetector. Figure 1a shows a schematic of the 0D/2D Ag_2Te/MoS_2 hybrid photodetector. We fabricated photodetectors capable of broadband IR detection by decorating MOCVD-grown MoS_2 field-effect transistors with colloidal Ag_2Te quantum dots, thereby forming a 0D/2D hybrid structure. Figure 1b plots the absorption spectrum of 1-dodecanethiol (DDT)-capped Ag_2Te QDs dispersed in tetrachloroethylene solution, showing clear excitonic absorption at 1457 nm with second and third excitonic peaks at 1258 and 950 nm, respectively. Fourier transform infrared spectroscopy (FTIR) analysis in Figure S5 confirms that the Ag_2Te QDs are predominantly capped with DDT, while the absorption coefficient (α) spectrum of Ag_2Te QD films in Figure S6 demonstrates strong broadband SWIR absorption, validating their effectiveness as an IR absorber for hybrid photodetector applications. As for the employed 2D material, MOCVD-grown MoS_2 film shows clear excitonic absorption at 657 nm and a cutoff wavelength of 680 nm in the visible range. The 0D/2D hybrid structure extends the absorption spectrum from 700 nm of MoS_2 to 1457 nm of Ag_2Te and opens a high-mobility MoS_2 channel from the Ag_2Te perspective. The particle size and distribution of the Ag_2Te QDs were determined through ultrahigh-resolution transmission electron microscopy (UHRTEM) analysis. The TEM images in Figure 1c indicate that the synthesized Ag_2Te QDs are spherical in shape and that the MOCVD-grown MoS_2 has a single-crystal lattice structure. The corresponding histogram in Figure S4a presents the particle size distribution, showing an average size of 4.4 ± 0.02 nm. To maximize gain at the 0D/2D hybrid interface, MoS_2 with ~3 μm grains was used for high mobility [36].

To determine the work function and valence band maximum of the colloidal Ag_2Te QDs and MOCVD-grown MoS_2, UPS measurements were conducted. The secondary electron cutoff and onset valence band regions of the UPS spectra acquired from Ag_2Te and MoS_2 are shown in Figures S4f and S7g, respectively. From the UPS work function measurement, a band diagram of the hybrid structure was obtained, as depicted in Figure 1d. Before the junction, the Ag_2Te and MoS_2 bands exhibit p-type and n-type semiconductor properties. After equilibrium, the built-in potential is 0.395 eV, and the difference between the conduction and valence bands is 0.33 and 0.79 eV. Under SWIR illumination, electrons generated in Ag_2Te QDs are transferred to the conduction band of MoS_2 in greater numbers than in the equilibrium state, while the built-in potential of the valence band confines holes. This electron transfer and confinement of holes have been analyzed in previous reports [37–40].

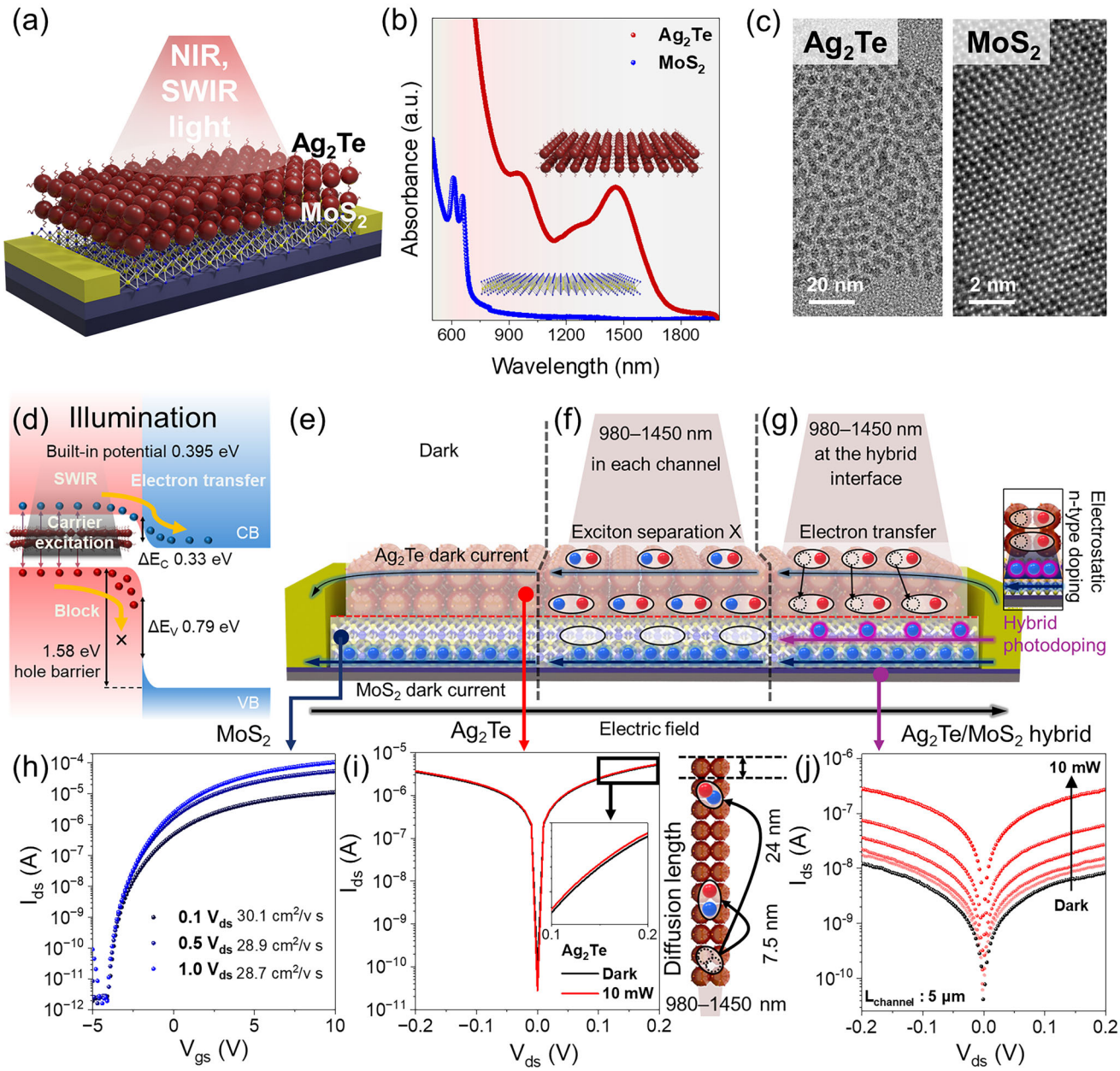

FIGURE 1 | Optical properties, band alignment, and photogenerated carrier characteristics. (a) Schematic illustration of the Ag_2Te/MoS_2 hybrid photodetector. (b) Absorption spectrum of colloidal Ag_2Te quantum dots (QDs) dispersed in tetrachloroethylene solvent and large-scale MoS_2 film. (c) UHRTEM images of colloidal Ag_2Te QDs and metal–organic chemical vapor deposition (MOCVD)-grown MoS_2. (d) Band alignment of the Ag_2Te/MoS_2 hybrid structure under illumination of short-wave infrared (SWIR) light. (e–g) Hybrid photodetector operation mechanism, showing dark current (e), exciton separation of each 0D/2D channel (f), and the photodoping effect at the 0D/2D interface (g). (h) Mobility characteristics of an MOCVD-grown MoS_2 transistor. (i) Ag_2Te conductance and 980 nm exciton separation/diffusion characteristics as a function of exciton lifetime. (j) Photodoping effect in the Ag_2Te/MoS_2 hybrid photodetector as a function of optical power at 980 nm.

Importantly, in this work, we designed the detailed operating mechanism of the current setup from the hybrid gain perspective. Figure 1e–g depicts the gain phenomenon through exciton lifetime and charge transfer in the 0D/2D Ag_2Te/MoS_2 hybrid photodetector. The gain equation is as follows:

$$G = \frac{\tau_{lifetime}}{\tau_{transit}} = \frac{\tau_{lifetime}}{L^2}\,\mu V_{ds},$$

where $\tau_{lifetime}$ is the carrier lifetime, $\tau_{transit}$ is the carrier transit time, L is the channel length, μ is the carrier mobility, and V_{ds} is the drain–source voltage. First, to achieve high gain, high charge mobility channels of MoS_2 are required. Figure 1h shows a transfer curve of an MOCVD-grown MoS_2 transistor with an Al_2O_3 dielectric layer. As a function of 0.1, 0.5, and 1 V_{ds}, the linear mobilities correspond to 30.1, 28.9, and 28.7 cm^2/V S. As the V_{ds} bias increases, the mobility decreases slightly but is consistent within 10%. As shown in Figure 1i, the 0.85 eV narrow

bandgap of Ag_2Te has a high conductance (G) of 2.6×10^5 S at 0.2 V_{ds}. When Ag_2Te QDs are decorated on the MoS_2 transistor channel, the relatively low conductance of MoS_2 can drag the total resistance of the hybrid structure down, in parallel with Ohm's law. Also, Ag_2Te QDs have a short exciton lifetime of 2.2 ns and limited carrier mobility of 0.01 cm^2/V S, according to a previous reference [41], and Ag_2Te film does not exhibit prominent photocurrent under 980 nm, as shown in the inset of Figure 1i. Assuming short exciton lifetimes of 2.2 to 22 ns, the diffusion lengths can reach 7.5 to 24 nm. The diffusion length equation is as follows:

$$Diffusion\ length\ (L_D) = \sqrt{D\tau_{lifetime}},$$

$$Diffusion\ coefficient\ (D) = \mu\frac{k_B T}{q},$$

where $\tau_{lifetime}$ is the exciton lifetime, μ is the carrier mobility, k_B is the Boltzmann coefficient, T is the temperature, and q is the elementary charge. As mentioned above, the size of one QD was measured here to be 4.4 nm, and thus in the film, no more than six QDs can be transported. Because of this limitation, photocurrent is rarely observed in QD films. While 980 and 1450 nm light generate sufficient excitons in the Ag_2Te channel, most excitons do not contribute to the photocurrent but rather recombine and disappear, as shown in Figure 1f. Meanwhile, the MoS_2 channel cannot generate excitons below 980 and 1450 nm, which are above the cutoff wavelength of 680 nm. In each channel, excitons generated by 980–1450 nm illumination cannot move to the electrode and recombine themselves in the material. Therefore, photo-induced current is not observed in either channel. In contrast, our previous studies revealed that interfacial spacing at the 0D/2D junction was consistently below 2–3 nm, which is markedly shorter than the minimum diffusion length of Ag_2Te, estimated to be 7.5 nm [42, 43]. Photo-induced electrons of the QDs can transfer to MoS_2 via the short interface gap. Under illumination of the 0D/2D hybrid interface at 980 and 1450 nm, holes trapped in the Ag_2Te QDs induce an electric field that modulates the MoS_2 electron channel, as shown in Figure 1g, a phenomenon referred to as the photodoping effect. Figure 1j shows a prominent photodoping behavior (upper first order) of the Ag_2Te/MoS_2 hybrid as a function of 980 nm power intensity. Figure S10 shows the drain current and photocurrent characteristics of hybrid devices under 1450 nm laser illumination, corresponding to the SWIR region. Although the individual channels of Ag_2Te and MoS_2 cannot generate photocurrent, the 0D/2D interface is the key driver that can induce strong photocurrent modulation by the photodoping effect. As a result, the hybrid structure achieves remarkably high photodetection responsivity, as discussed below, exceeding the performance limits typically observed in conventional low-dimensional photodetectors [39].

In SWIR photodetectors, the requirement for narrow-bandgap materials to enable long-wavelength absorption has inherently led to thermally induced high dark currents, which in turn limit the achievable detectivity. Detectivity is determined using the flicker noise current (i_{FN}) according to the equation $D^* = R\sqrt{A}/i_{FN}$, where R is the responsivity of the device (given by $R = I_{photo}/P_{incident}$), A is the active area of the device, and i_{FN} represents the flicker noise. Figure S13b presents the measured dark current of the 0D/2D Ag_2Te/MoS_2 hybrid photodetector as a function of channel length, recorded over a 2 s interval with a temporal resolution of 0.0001 s. A clear linear decrease in dark current is observed with increasing channel length, ranging from 0.25×10^{-6} to 0.74×10^{-6} A. The dark current signal recorded over 2 s was transformed into a noise-power-density spectrum via fast Fourier transform analysis, revealing a flicker-noise-dominated behavior ($A^2\ Hz^{-1}$), as shown in Figure S13a. Figure 2a further presents the frequency-dependent noise current for Ag_2Te/MoS_2 hybrid photodetectors with channel lengths ranging from 2 to 5 μm. The measured noise current decreases systematically with increasing channel length across the entire frequency range, directly reflecting the reduction in dark current observed in Figure S13b. At higher frequencies, the noise spectrum exhibits a gradual tendency toward flattening, indicating convergence toward the calculated shot-noise floor. The characteristic 1/f behavior is clearly observed in the low-frequency region, and the calculated shot-noise current levels are included for comparison. These results highlight the direct correlation between channel scaling and suppression of low-frequency noise (10^{-19} A^2 Hz level at 1 Hz) in the hybrid device.

According to the gain equation, the photodetector gain decreases sharply with increasing channel length, following a $1/L^2$ dependence. Based on the previously reported exciton lifetime of Ag_2Te, Figure 2b illustrates the relationship between exciton diffusion length and hybrid gain as a function of channel length. To achieve exciton diffusion lengths of 2, 3, 4, and 5 μm, progressively longer exciton lifetimes are required. When both conditions above are satisfied, the gain of our 0D/2D Ag_2Te/MoS_2 hybrid photodetector is calculated to be 7.8, as shown by the colored arrow in Figure 2b. In practice, it is not feasible for the exciton lifetime to increase proportionally to the required condition as the channel length increases. To investigate both scenarios, namely where the exciton diffusion length exceeds the channel length and where this condition is not met, we analyzed the time-resolved photocurrent dynamics, as shown in Figure 2c–f. Figure 2c,d exhibit a 'shark tail' profile in which hole trapping increases over time, leading to a gradual enhancement of the photodoping effect. Due to the accumulation of hole traps, the shark tail effect resulted in slow photoresponse times, measured as 452 ms at a channel length of 2 μm and 303 ms at 3 μm. In contrast, Figure 2e,f display a 'peak tail' profile where the longer channel length favors a faster electron–hole recombination rate, counterbalancing the accumulation of trapped holes. As evidence, an instantaneous current peak is observed at the moment electrons transfer from Ag_2Te to MoS_2, followed by a gradual convergence of the current, which is attributed to the photodoping effect. The balance between hole trapping and appropriate recombination yielded the peak tail effect, resulting in relatively fast photoresponse times of 34 ms at a channel length of 4 μm and 13 ms at 5 μm. Figure S12 demonstrates the reliability of the photodetector through five repeated photoresponse cycles.

To evaluate the performance of the Ag_2Te/MoS_2 hybrid photodetector, responsivity and detectivity were calculated, as shown in Figure 2g,h. The responsivity R of the 0D/2D hybrid photodetector was calculated using the following equation based on measured changes in photocurrent and illumination powers: $R = \frac{(I_{illuminated} - I_{dark})}{P}$, where $I_{illuminated}$ and I_{dark} are the currents

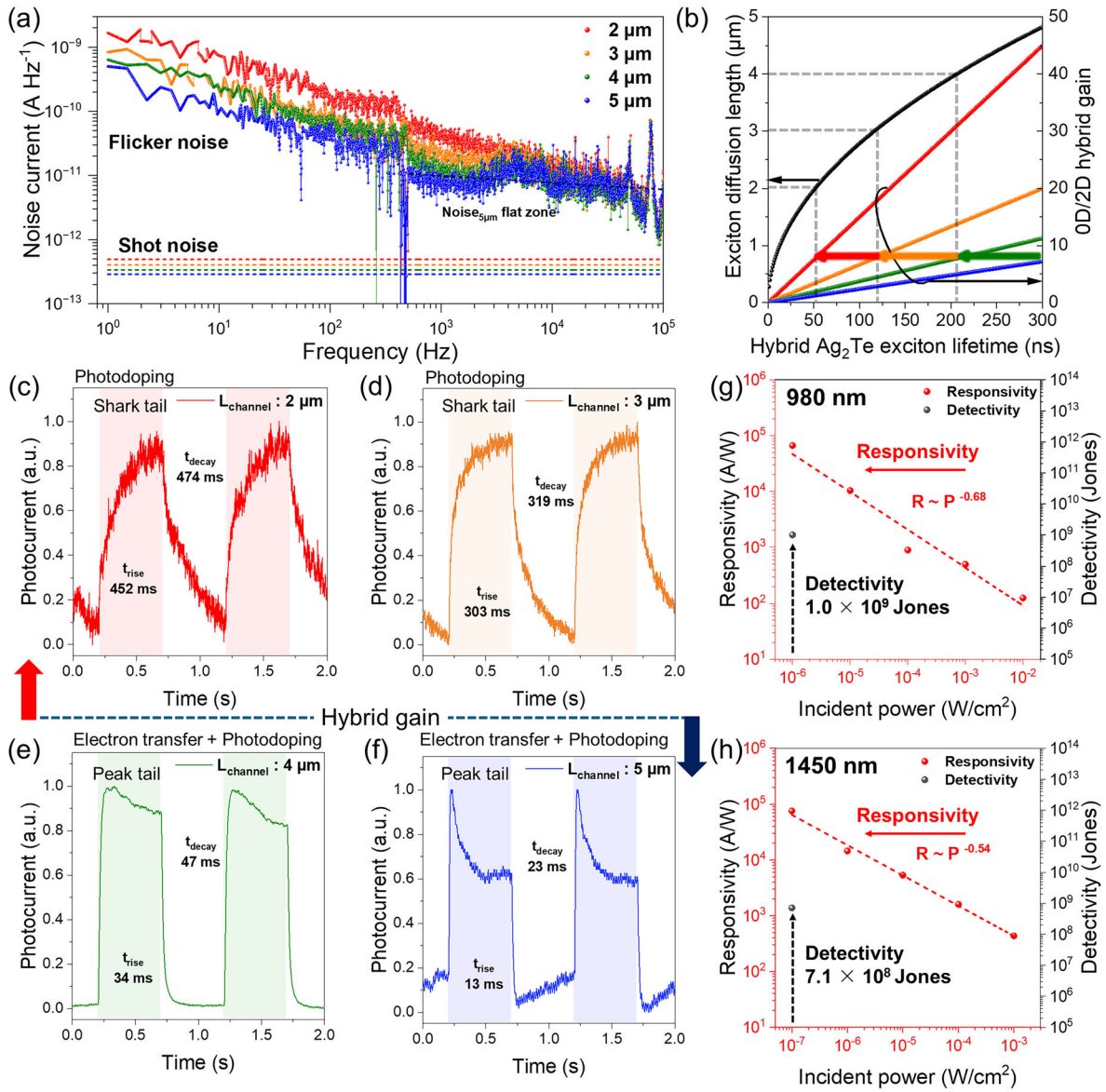

FIGURE 2 | Photodoping and photoresponse characteristics under 980 and 1450 nm illumination. (a) Frequency-dependent noise current of Ag_2Te/MoS_2 hybrid photodetectors with different channel lengths (2–5 μm), exhibiting characteristic flicker (1/f) behavior. The calculated shot-noise current levels are included for comparison. (b) 0D/2D hybrid gain and exciton diffusion length as a function of channel length (2–5 μm) with a Ag_2Te exciton lifetime reference range from 2 to 300 ns. (c–f) Photoresponse time and response behavior of the Ag_2Te/MoS_2 hybrid photodetector as a function of channel length (2–5 μm) under 980 nm laser illumination. The (c) and (d) panels show a 'shark tail' profile, while (e) and (f) show a 'peak tail' profile. (g,h) Responsivity and detectivity of the Ag_2Te/MoS_2 hybrid photodetector with a 5 μm channel length under 980 nm (h) and 1450 nm (i) illumination.

measured under incident light and in a dark state, respectively, and P is the applied power to the photodetector. The responsivities were calculated to be 6.6×10^4 AW^{-1} for the 980 nm laser and 1.4×10^4 AW^{-1} for the 1450 nm laser at an illumination power of 1 μW/cm^2. In particular, a responsivity value of 7.5×10^4 AW^{-1} was obtained for 1450 nm at 100 nW/cm^2 illumination power. As the other key advantage of the developed photodetector, its specific detectivity D^* was calculated by considering both shot noise and flicker noise limits, expressed by the following equations:

(with shot noise)

$$D^* = \frac{R\sqrt{A}}{I_{SN}},$$

(with flicker noise)

$$D^* = R\sqrt{A}/I_{FN}$$

Here, the shot noise current is $I_{SN} = \sqrt{2eI_{dark}}$ where e is the electron charge, A is the active area, and i_{FN} is the flicker noise current. The specific detectivities calculated from I_{SN} and I_{FN} were compared, as shown in Figure S10g,h. In this work, the detectivity calculated using the experimentally measured flicker noise is presented as the device's specific detectivity, representing the actual experimental performance. In contrast, the detectivity estimated using the shot-noise expression is included only as the shot-noise-limited theoretical upper bound. The difference

between the approaches was two orders of magnitude, and this was consistent for both 980 and 1450 nm lasers. When calculated based on shot noise, photodetectivity values of up to 9.4×10^{11} Jones were confirmed at 100 nW/cm^2 with the 1450 nm laser and up to 8.32×10^{11} Jones at 1 μW/cm^2 with the 980 nm laser. Using flicker noise at the same power, the detectivity was 7.14×10^8 Jones with the 1450 nm laser and 9.98×10^8 Jones with the 980 nm laser, respectively. The two methods differ in their definition and handling of noise, and the choice of method depends on the device's usage environment and performance requirements. The overall behavior profiles of responsivity, shot-noise-limited detectivity, and flicker-noise-limited detectivity for different channel lengths are shown in Figures S13 and S14. To design the most efficient hybrid photodetector, considering the key figures of merit of responsivity, detectivity, and response time, we optimized the device structure to take advantage of trap- and defect-mediated transport dynamics. Notably, this architecture applies to CMOS integration and offers strong potential for seamless coupling with ROICs, paving the way for scalable, high-performance imaging systems.

Next, we designed a sensor array for IR imaging based on the developed hybrid structure; the related fabrication steps and structural configuration are illustrated in Figure 3. The schematic representation of the device architecture shows Ag_2Te QDs integrated onto monolayer MoS_2 to form a SWIR sensing unit. Interdigitated source and drain electrodes extend the photodoping-active area while maintaining high spatial resolution across the sensing region. The detailed fabrication process is presented in Figure 3a. In step 1, large-area monolayer MoS_2 films are synthesized on SiO_2/Si substrates via MOCVD, producing a uniform and crystalline channel material across the wafer. To facilitate film transfer, in step 2 a polymethyl methacrylate (PMMA) support layer is spin-coated onto the as-grown MoS_2 surface, followed by lamination of thermal release tape (TRT) onto the PMMA/MoS_2/SiO_2/Si stack in step 3, enabling subsequent detachment of the film without chemical etchants. In step 4, deionized (DI) water-assisted delamination of the MoS_2 layer is performed that results in an intact MoS_2/PMMA/TRT film, as shown in step 5, free from chemical contamination. The sensor array is then formed by first patterning source and drain electrodes in a crossbar layout and dry-transferring the film to the fabricated array, as shown in step 6. After MoS_2 transfer onto the patterned substrate, active channel definition is achieved via standard photolithography and reactive ion etching (RIE) to isolate individual device pixels, as illustrated in step 7. In step 8, Ag_2Te QDs are spin-coated onto the patterned MoS_2 channels, creating the 0D/2D heterojunctions that serve as photoactive regions. This scalable fabrication approach enables uniform integration of 0D and 2D materials across the entire array. Finally, in step 9 the array chip is mounted onto a printed circuit board (PCB), and electrical connections are established by wire bonding.

The completed device, as shown in Figure 3b, consists of a 32×32 pixel array corresponding to 1024 individually addressable hybrid photodetectors. The array is organized with 16 parallel source lines and 16 orthogonal drain lines, an arrangement that enables efficient multiplexed addressing while minimizing parasitic resistance and capacitance. Figure 3c presents an optical micrograph of the array, clearly revealing the precise patterning of MoS_2 channels within each pixel. The high-magnification view in Figure 3d provides a detailed look at the structural components of a single device unit, where the active MoS_2 channel region is defined between the source and drain electrodes. To electrically isolate adjacent lines and prevent short-circuiting, a HfO_2 dielectric layer was introduced. Figure S15 shows an optical microscope image and CAD layout of the fabricated array, illustrating its dense grid pattern and uniform pixel arrangement, and Figure S16 presents the array layout and architecture design, detailing each component pattern. This architecture allows for large-scale, high-uniformity integration of nanoscale hybrid photodetectors, offering both scalability and compatibility with standard PCB-based readout electronics. The integration of Ag_2Te QDs onto MoS_2 channels enables broadband detection capability, particularly in the SWIR regime, while the planar pixel arrangement supports future expansion to high-resolution imaging arrays. Each pixel operates as an individual photodetector, formed at the intersection of horizontally aligned drain lines and vertically aligned source lines. Such a crossbar architecture enables efficient pixel-level addressing and signal readout. The precise integration of these elements is essential for ensuring high sensitivity and uniformity across the entire sensor array.

The baseline performance of the photodetector was first examined in a single-pixel scanning experiment with a USAF resolution target, as shown in Figure 4a. Line-by-line raster acquisition successfully reconstructed the 2D image, although minor temporal artifacts, such as trailing were observed during mechanical translation. These artifacts were progressively mitigated through soft-min fusion, unsharp masking, and gamma correction, as detailed in Figure S17, yielding improved interpretability without introducing artificial features. This result demonstrates that even a single detector possesses sufficient spatial selectivity for high-resolution imaging and establishes a benchmark for subsequent array development [44–46].

The hybrid 32×32 Ag_2Te/MoS_2 array was then interfaced through a multiplexer-enabled circuit configuration (Figure 4b), which automated column-wise readout while maintaining stable photocurrent sampling at each addressed pixel. A 3D schematic of the IR imaging setup is shown in Figure 4c, where the features of the transmission mask define the structured illumination projected onto the array. Distinct spatial responses were reproduced across the array, with particularly strong contrast observed in peripheral regions. Post-processing corrections, including dark current suppression and row-level interpolation, further enhanced uniformity and artifact suppression, as seen in Figure S18.

To evaluate directional robustness, as shown in Figure 4d four sets of response maps were recorded at 90° rotation intervals. Each map reproduced the illumination pattern with consistent edge definition, while minor orientation-dependent variations enriched the overall spatial representation. A schematic overview of the full correction and fusion pipeline is summarized in Figure S19.

Finally, composite images were generated by comparing two pixel-wise fusion strategies. Averaging across the four rotated acquisitions produced smooth gradients but blurred fine details,

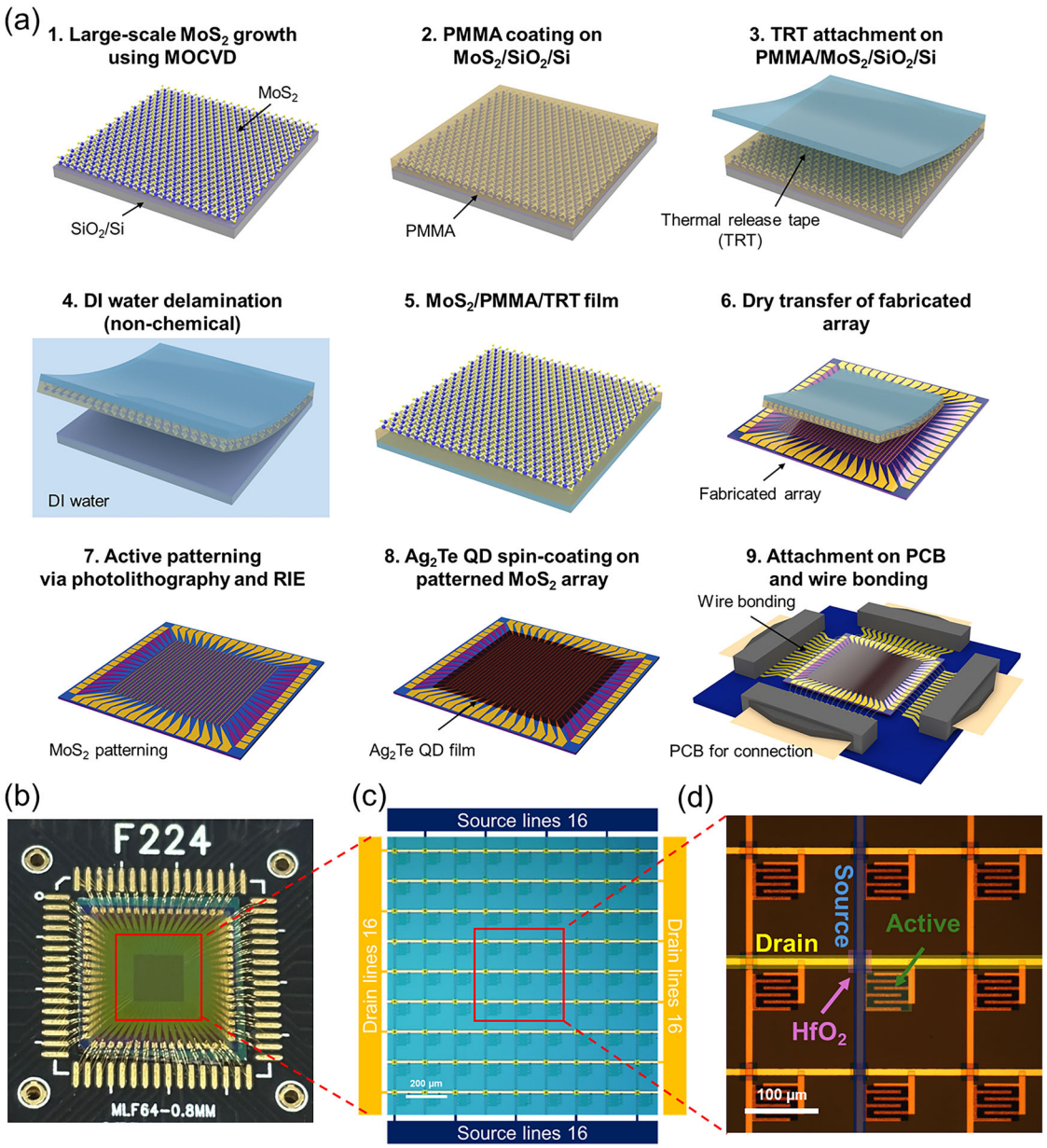

FIGURE 3 | Fabrication details of the Ag_2Te/MoS_2 hybrid sensor array. (a) Fabrication process of the Ag_2Te/MoS_2 hybrid sensor array. (b) Optical image of the fully fabricated sensor chip with wire bonding on a printed circuit board (PCB) for external connection. (c) Optical image showing a simplified representation of the 32 × 32 sensor array layout with periodically arranged device units. (d) Magnified optical image highlighting the key components of a single device unit, including source and drain electrodes, HfO_2 gate dielectric, and the MoS_2 active channel region.

whereas maximum-value fusion preserved edge contrast and structural sharpness, as in Figure S20. Based on its superior clarity, the maximum-value strategy was adopted to synthesize the final image shown in Figure 4e, which demonstrates high-fidelity reproduction of complex illumination patterns and confirms the scalability of the array platform for structured IR imaging.

3 | Conclusion

In summary, we have mitigated the trade-off between gain and photoresponse speed in SWIR photodetectors by systematically modulating the channel length. By adopting an optimized 5 μm channel length in the developed 0D/2D Ag_2Te/MoS_2 hybrid architecture, this work provides a promising strategy that may pave the way for next-generation, high-performance SWIR photodetectors. The design delivers broadband absorption, high responsivity, and exceptional detectivity in a scalable platform. Through the integration of long-wavelength-absorbing Ag_2Te quantum dots with high-mobility MoS_2 channels, our structure induces a strong photodoping effect that is absent in the individual components, enabling pronounced photocurrent modulation at 980 and 1450 nm. The optimized hybrid design achieved responsivity up to 7.5×10^4 AW^{-1} and detectivity exceeding 9.9×10^8 Jones, while channel-length engineering and controlled trap recombination dynamics reduced the photoresponse time to tens of milliseconds. Furthermore, the

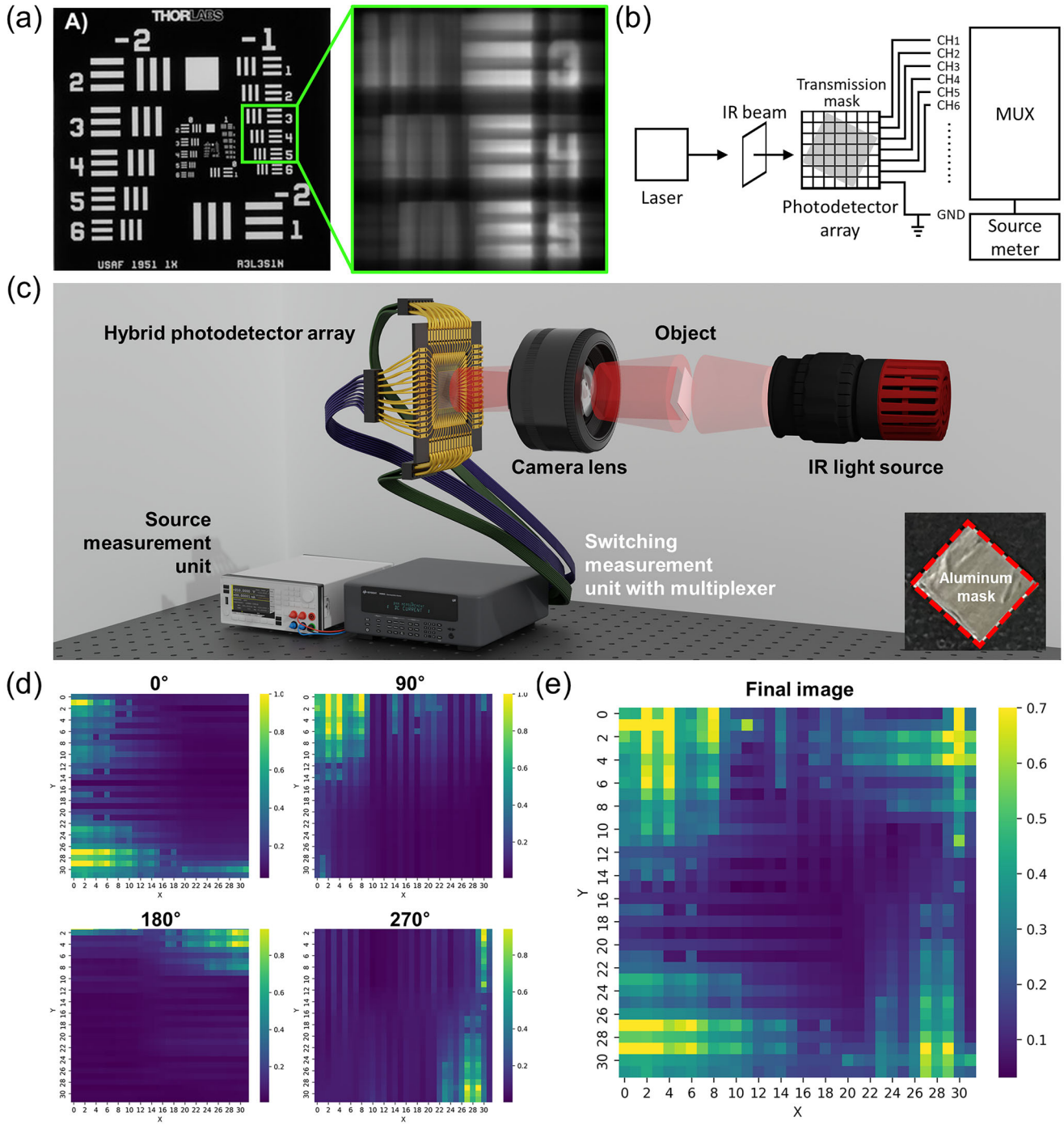

FIGURE 4 | Hybrid infrared imaging system and results. (a) Single-pixel infrared imaging of the USAF resolution target using a scanning-based approach. The object corresponds to elements 3, 4, and 5 in group −1, spanning approximately 1.4 × 1.5 cm^2. The inset shows a magnified view of the visualized region. (b) Circuit diagram of the proposed photodetector array system. (c) Schematic illustration of the imaging setup. (d) Normalized response maps acquired at four angular configurations (0°, 90°, 180°, and 270°). (e) Final image synthesized from the four angular response maps.

fabrication of a wafer-scale 32 × 32 pixel array for IR imaging was shown to ensure high spatial uniformity, low-noise readout, and compatibility with CMOS back-end processes. This hybrid material strategy not only achieves ~10^5 AW^{-1} levels by utilizing high-gain based photodoping but also provides a viable pathway toward high-resolution, SWIR-capable imaging systems that can be seamlessly integrated into next-generation ROIC platforms.

4 | Experimental Section

4.1 | Synthesis of Ag_2Te Quantum Dots

Ag_2Te quantum dots (QDs) were synthesized using a previously reported colloidal method. Silver and tellurium precursors were prepared under an inert atmosphere and reacted in a mixture of oleylamine and octadecene at elevated temperature. After

completion of the reaction, the QDs were purified by repeated precipitation and redispersion and stored in toluene under a nitrogen atmosphere for further use. Detailed synthesis procedures and purification steps are provided in the Supporting Information.

4.2 | Growth of Few-Layer MoS_2

Few-layer MoS_2 was grown on substrates by metal–organic chemical vapor deposition (MOCVD) in a hot-wall quartz tube furnace. Metal–organic molybdenum and sulfur precursors were introduced under reduced pressure, and NaCl was used as a growth promoter to enhance grain size. The growth conditions were optimized to obtain continuous few-layer MoS_2 films.

4.3 | Fabrication of Ag_2Te/MoS_2 Hybrid IR Sensor Arrays

Ag_2Te/MoS_2 hybrid IR sensor arrays were fabricated using a similar process as above. Word and bit line electrodes were patterned on Al_2O_3-coated Si substrates, and a HfO_2 insulating layer was introduced to prevent electrical shorting. MoS_2 was transferred and annealed, followed by spin-coating of Ag_2Te QDs to complete the hybrid sensor array. Further details regarding array fabrication and insulation processes are available in the Supporting Information.

Author Contributions

S.-J. Jeong carried out device fabrication, performed charge transport measurements, analyzed the data, and wrote the paper; H.W. Ko and S. Jo contributed equally to this work. H.W. Ko designed the overall imaging system, conducted imaging experiments, and contributed to manuscript preparation. S. Jo assisted with imaging experiments and co-wrote the manuscript. J.-M. Kim and Y. Kim carried out measurements. J. Selvaraj, J.-H. Ahn, H. Lee, S. Jeong, and H. Kim carried out spectroscopy. N. Lee carried out device fabrication. P.H. Seo and J.W. Shim participated in the imaging experiments and assisted in data analysis. M.-C. Park supervised the overall imaging-related experiments, provided technical guidance, and reviewed the manuscript. J.-S. Lee and H.-S. Ra conceived and designed the experiments, helped with measurements, analyzed the data, and co-wrote the paper. All authors discussed the results and commented on the manuscript.

Acknowledgements

This work was supported by the National Research Foundation of Korea (NRF) grant (2022R1A2C2008278) and the National Research Council of Science & Technology (NST) grant (No. CAP 23071–300) funded by the Korea government (MSIT) and the Korea Institute of Science and Technology (KIST) Institutional Program (Grant No. 2E33542) and the Technology Innovation Program (Grant No. 02316245) funded by the Ministry of Trade, Industry and Energy (MOTIE, Korea). This work was also supported by the Korean government (MSIT) (No. GTL24041-000) and the Ministry of Science and ICT, Korea (RS-2025-23323225). This work was supported by the Technology Innovation Program (RS-2025-04812973, Neuro-Semi-AI Fusion Superhuman Project: A Platform for Augmenting Physical Abilities Based on Central Nervous System Stimulation) funded by the Ministry of Trade, Industry & Energy (MOTIE, Korea).

Conflicts of Interest

The authors declare no conflicts of interest.

Data Availability Statement

The data that support the findings of this study are available from the corresponding author upon reasonable request.;

References

1. I. Moreels, Y. Justo, B. De Geyter, K. Haustraete, J. C. Martins, and Z. Hens, "Size-Tunable, Bright, and Stable PbS Quantum Dots: A Surface Chemistry Study," *ACS nano* 5, no. 3 (2011): 2004–2012.

2. D. V. Talapin, J.-S. Lee, M. V. Kovalenko, and E. V. Shevchenko, "Prospects of Colloidal Nanocrystals for Electronic and Optoelectronic Applications," *Chemical reviews* 110, no. 1 (2010): 389–458.

3. Y. Zhang, H. Yang, X. An, et al., "Controlled Synthesis of $Ag_2Te@Ag_2S$ Core–Shell Quantum Dots With Enhanced and Tunable Fluorescence in the Second Near-Infrared Window," *Small* 16, no. 14 (2020): 2001003.

4. Y. Zhou, B. Huang, S.-H. Chen, S.-L. Liu, M. Zhang, and R. Cui, "Ultra-Bright Near-Infrared-IIb Emitting Zn-Doped Ag_2Te Quantum Dots for Noninvasive Monitoring of Traumatic Brain Injury," *Nano Research* 16, no. 2 (2023): 2719–2727.

5. V. Pejović, E. Georgitzikis, J. Lee, et al., "Infrared Colloidal Quantum Dot Image Sensors," *IEEE Transactions on Electron Devices* 69, no. 6 (2021): 2840–2850.

6. L. Peng, Y. Wang, Y. Ren, Z. Wang, P. Cao, and G. Konstantatos, "InSb/InP Core–Shell Colloidal Quantum Dots for Sensitive and Fast Short-Wave Infrared Photodetectors," *ACS nano* 18, no. 6 (2024): 5113–5121.

7. S. A. McDonald, G. Konstantatos, S. Zhang, et al., "Solution-Processed PbS Quantum Dot Infrared Photodetectors and Photovoltaics," *Nature materials* 4, no. 2 (2005): 138–142.

8. H. Lu, G. M. Carroll, N. R. Neale, and M. C. Beard, "Infrared Quantum Dots: Progress, Challenges, and Opportunities," *ACS nano* 13, no. 2 (2019): 939–953.

9. Y. Cao, A. Stavrinadis, T. Lasanta, D. So, and G. Konstantatos, "The Role of Surface Passivation for Efficient and Photostable PbS Quantum Dot Solar Cells," *Nature Energy* 1, no. 4 (2016): 1–6.

10. H. Yang, H. Huang, X. Ma, et al., "Au-Doped Ag_2 Te Quantum Dots With Bright NIR-IIb Fluorescence for In Situ Monitoring of Angiogenesis and Arteriogenesis in a Hindlimb Ischemic Model," *Advanced Materials* 33, no. 37 (2021): 2103953.

11. M. H. Hudson, M. Chen, V. Kamysbayev, et al., "Conduction Band Fine Structure in Colloidal HgTe Quantum Dots," *ACS nano* 12, no. 9 (2018): 9397–9404.

12. H. Seo, H. J. Eun, A. Y. Lee, H. K. Lee, J. H. Kim, and S. W. Kim, "Colloidal InSb Quantum Dots for 1500 nm SWIR Photodetector With Antioxidation of Surface," *Advanced Science* 11, no. 4 (2024): 2306439.

13. M. Bernechea, N. Cates, G. Xercavins, D. So, A. Stavrinadis, and G. Konstantatos, "Solution-Processed Solar Cells Based on Environmentally Friendly $AgBiS_2$ Nanocrystals," *Nature Photonics* 10, no. 8 (2016): 521–525.

14. I. Burgués-Ceballos, Y. Wang, and G. Konstantatos, "Mixed $AgBiS_2$ Nanocrystals for Photovoltaics and Photodetectors," *Nanoscale* 14, no. 13 (2022): 4987–4993.

15. P. E. Malinowski, E. Georgitzikis, J. Maes, et al., "Thin-Film Quantum Dot Photodiode for Monolithic Infrared Image Sensors," *Sensors* 17, no. 12 (2017): 2867.

16. J. Ouyang, N. Graddage, J. Lu, et al., "Ag_2Te Colloidal Quantum Dots for Near-Infrared-II Photodetectors," *ACS Applied Nano Materials* 4, no. 12 (2021): 13587–13601.

17. G. Kim, D. Choi, S. Y. Eom, H. Song, and K. S. Jeong, "Extended Short-Wavelength Infrared Photoluminescence and Photocurrent of

Nonstoichiometric Silver Telluride Colloidal Nanocrystals," *Nano Letters* 21, no. 19 (2021): 8073–8079.

18. G. Kim, D. Choi, S. Y. Eom, et al., "Extended Short-Wavelength Infrared Ink by Surface-Tuned Silver Telluride Colloidal Quantum Dots and Their Infrared Photodetection," *ACS Materials Letters* 6 (2024): 4988–4996.

19. Y. Wang, L. Peng, J. Schreier, et al., "Silver Telluride Colloidal Quantum Dot Infrared Photodetectors and Image Sensors," *Nature Photonics* 18, no. 3 (2024): 236–242.

20. A. K. Geim and K. S. Novoselov, "The Rise of Graphene," *Nature Materials* 6, no. 3 (2007): 183–191.

21. B. Radisavljevic, A. Radenovic, J. Brivio, V. Giacometti, and A. Kis, "Single-Layer MoS_2 Transistors," *Nature nanotechnology* 6, no. 3 (2011): 147–150.

22. F. Li, D. Benetti, M. Zhang, J. Feng, Q. Wei, and F. Rosei, "Modulating the 0D/2D Interface of Hybrid Semiconductors for Enhanced Photoelectrochemical Performances," *Small Methods* 5, no. 8 (2021): 2100109.

23. S. Sinha, H. Kim, and A. W. Robertson, "Preparation and Application of 0D-2D Nanomaterial Hybrid Heterostructures for Energy Applications," *Materials Today Advances* 12 (2021): 100169.

24. S. Mukherjee, S. Jana, T. Sinha, S. Das, and S. Ray, "Infrared Tunable, Two Colour-Band Photodetectors on Flexible Platforms Using 0D/2D PbS–MoS_2 Hybrids," *Nanoscale Advances* 1, no. 8 (2019): 3279–3287.

25. F. Wang, Y. Zhang, Y. Gao, et al., "2D Metal Chalcogenides for IR Photodetection," *Small* 15, no. 30 (2019): 1901347.

26. S. Joseph, J. Mohan, S. Lakshmy, et al., "A Review of the Synthesis, Properties, and Applications of 2D Transition Metal Dichalcogenides and Their Heterostructures," *Materials Chemistry and Physics* 297 (2023): 127332.

27. Y. Fang, Y. Ge, C. Wang, and H. Zhang, "Mid-Infrared Photonics Using 2D Materials: Status and Challenges," *Laser & Photonics Reviews* 14, no. 1 (2020): 1900098.

28. J. Zha, M. Luo, M. Ye, et al., "Infrared Photodetectors Based on 2D Materials and Nanophotonics," *Advanced Functional Materials* 32, no. 15 (2022): 2111970.

29. O. Ozdemir, I. Ramiro, S. Gupta, and G. Konstantatos, "High Sensitivity Hybrid PbS CQD-TMDC Photodetectors up to 2 μm," *Acs Photonics* 6, no. 10 (2019): 2381–2386.

30. N. Huo, S. Gupta, and G. Konstantatos, "MoS_2–HgTe Quantum Dot Hybrid Photodetectors Beyond 2 μm," *Advanced Materials* 29, no. 17 (2017): 1606576.

31. C. Zhang, L. Lian, Z. Yang, J. Zhang, and H. Zhu, "Quantum Confinement-Tunable Ultrafast Charge Transfer in a PbS Quantum Dots/WSe_2 0D–2D Hybrid Structure: Transition From the Weak to Strong Coupling Regime," *The Journal of Physical Chemistry Letters* 10, no. 24 (2019): 7665–7671.

32. N. Huo and G. Konstantatos, "Recent Progress and Future Prospects of 2D-Based Photodetectors," *Advanced Materials* 30, no. 51 (2018): 1801164.

33. G. Konstantatos, M. Badioli, L. Gaudreau, et al., "Hybrid Graphene–Quantum Dot Phototransistors With Ultrahigh Gain," *Nature nanotechnology* 7, no. 6 (2012): 363–368.

34. A. Chetia, J. Bera, A. Betal, and S. Sahu, "A Brief Review on Photodetector Performance Based on Zero Dimensional and Two Dimensional Materials and Their Hybrid Structures," *Materials Today Communications* 30 (2022): 103224.

35. J.-L. Meng, T.-Y. Wang, L. Chen, et al., "Energy-Efficient Flexible Photoelectric Device With 2D/0D Hybrid Structure for Bio-Inspired Artificial Heterosynapse Application," *Nano Energy* 83 (2021): 105815.

36. D. Kufer and G. Konstantatos, "Photo-FETs: Phototransistors Enabled by 2D and 0D Nanomaterials," *ACS Photonics* 3, no. 12 (2016): 2197–2210.

37. J.-M. Kim, S.-J. Jeong, H.-S. Kim, et al., "Direct Photo-Crosslinking Patterning for High-Performance 0D–2D Hybrid Photodetectors," *Advanced Optical Materials* 12, no. 35 (2024): 2401755.

38. B. Moon, J.-H. Ahn, M.-H. Jeong, S.-H. Lee, and J.-S. Lee, "High-Performance and Stability of $CsPbBr_3$/WSe_2 Hybrid Photodetectors Functionalized Using Quaternary Ammonium Ligands," *Advanced Optical Materials* 11, no. 17 (2023): 2300414.

39. H.-S. Ra, S.-H. Lee, S.-J. Jeong, S. Cho, and J.-S. Lee, "Advances in Heterostructures for Optoelectronic Devices: Materials, Properties, Conduction Mechanisms, Device Applications," *Small Methods* 8, no. 2 (2024): 2300245.

40. S.-J. Jeong, S. Cho, B. Moon, et al., "Zero Dimensional–Two Dimensional Hybrid Photodetectors Using Multilayer MoS_2 and Lead Halide Perovskite Quantum Dots With a Tunable Bandgap," *ACS Applied Materials & Interfaces* 15, no. 4 (2023): 5432–5438.

41. Y. Wang, H. Wu, C. Rodà, et al., "Shortwave Infrared Light Detection and Ranging Using Silver Telluride Quantum Dots," *Advanced Materials* 37, no. 21 (2025): 2500977.

42. H.-S. Ra, T. W. Kim, D. A. Taylor, et al., "Probing Optical Multi-Level Memory Effects in Single Core-Shell Quantum Dots and Application Through 2D–0D Hybrid Inverters," *Advanced Materials* 35, no. 39 (2023): 2303664.

43. A. Y. Lee, H.-S. Ra, D.-H. Kwak, et al., "Hybrid Black Phosphorus/Zero-Dimensional Quantum Dot Phototransistors: Tunable Photodoping and Enhanced Photoresponsivity," *ACS Applied Materials & Interfaces* 10, no. 18 (2018): 16033–16040.

44. T. H. Kim, B.-S. Yu, H. W. Ko, et al., "Self-Powering Sensory Device With Multi-Spectrum Image Realization for Smart Indoor Environments," *Advanced Materials* 36, no. 2 (2024): 2307523.

45. S. Oh, S. Jo, J. H. Lee, et al., "Robust Imaging Through Light-Scattering Barriers via Energetically Modulated Multispectral Organic Photodetectors," *Advanced Materials* 37 (2025): 2503868.

46. J. Jang, J. P. Hong, S.-J. Kim, et al., "Conductive-Bridge Interlayer Contacts for Two-Dimensional Optoelectronic Devices," *Nature Electronics* 8 (2025): 1–11.

Supporting Information

Additional supporting information can be found online in the Supporting Information section.

Supporting File: adma72856-sup-0001-SuppMat.docx.